Transition from flat-band localization to Anderson localization: Realization and characterization in a one-dimensional momentum lattice

Yi-Yi Mao ,[1,2] Chao Zeng,[1,2,3] Yue-Ran Shi,[4,5] Fei-Fei Wu,[1,2] Yan-Jun Xie,[1,2] Tao Yuan,[1,2] Wei Zhang,[4,5,*]
Han-Ning Dai ,[1,2,3,†] Yu-Ao Chen,[1,2,3] and Jian-Wei Pan[1,2,3]

[1]*Hefei National Research Center for Physical Sciences at the Microscale and School of Physical Sciences, University of Science and Technology of China, Hefei 230026, China*

[2]*Shanghai Research Center for Quantum Sciences and CAS Center for Excellence in Quantum Information and Quantum Physics, University of Science and Technology of China, Shanghai 201315, China*

[3]*Hefei National Laboratory, University of Science and Technology of China, Hefei 230088, China*

[4]*Department of Physics and Beijing Key Laboratory of Opto-electronic Functional Materials and Micro-nano Devices, Renmin University of China, Beijing 100872, China*

[5]*Key Laboratory of Quantum State Construction and Manipulation (Ministry of Education), Renmin University of China, Beijing 100872, China*

The diffusion and localization of particles in lattice potentials are essential topics in the study of quantum states of matter. As two distinct mechanisms, flat-band localization (FBL) caused by destructive interference and Anderson localization (AL) by strong disorder can both prohibit particle transport and lead to an insulator state. The realization and characterization of the two different insulating phases necessitate the ability to shape the lattice potential and measure particle transport at the single-site level. By using spatial momentum as an artificial dimension, ultracold quantum gas in a momentum lattice provides an ideal platform to achieve single-site resolution. Here, we demonstrate that the transition from flat-band localization to Anderson localization can be realized and quantitatively studied in a Bose-Einstein condensate in a one-dimensional momentum lattice. The flat-band localization is realized in a one-dimensional Tasaki model, while the transition to Anderson localization is achieved by imposing a strong enough disorder potential and is characterized by stark features of particle transport from an initial state in an experimentally realistic finite-size system. Submitted in parallel with Zeng *et al.*, this article provides experimental details on the realization of an effective model and preparation of the initial state as well as a theoretical study of the transition with experimental parameters.

I. INTRODUCTION

The manipulation of the lattice potential and detection of transport behavior at a single-site resolution have long been pursued in the study of quantum states of matter. In condensed matter physics, exciting progress in scanning probe microscopy has played a vital role in the study of the surface properties of superconductors, magnetic materials, ferroelectric devices, and two-dimensional layered materials [1]. However, the control of lattice potential at a single-site level is quite challenging in solid-state samples. Ultracold quantum gases of neutral atoms offer another possibility to achieve these two demands. With the aid of technical advances in atom assembly, atoms can be arranged in a wide range of configurations in microtraps by optical tweezer arrays [2,3], spatial light modulators [4], and digital micromirror devices [5,6]. Detection of atoms with single-site resolution has also been achieved via carefully designed imaging systems with large numerical aperture [7,8].

The momentum lattice provides an ideal platform to simultaneously realize lattice shaping and particle detection at a single-site level, where different momenta are used to represent synthetic sites. By driving multiple Bragg processes between designated momentum states, we can easily tune each site by adjusting the corresponding laser parameters, including the frequency, intensity, and phase [9–11]. With these advantages, momentum lattice has been used to study topological properties [12–14], chiral dynamics [10,15], and time boundary effects [16]. In particular, in the experimental works by Li [17] and Zeng [18], a momentum lattice is used to tailor decorated lattices with a perfectly flat band, where the inverse Anderson transition and the transition from flat-band localization (FBL) to Anderson localization (AL) are realized and extensively studied. As two distinct mechanisms of localization, the study of FBL and AL has attracted much attention. The existence of strong disorder suppresses the propagation of waves, resulting in traditional Anderson localization [19,20]. Meanwhile, in a flat-band system, the perfect destructive interference of particle hopping can result in a different type of localization known as flat-band localization [21–23]. The localization properties are maintained under finite interaction strength for both AL and FBL, known as many-body localization [24,25]. However, the many-body localization states that emerged from FBL and AL are distinct phases with different physical properties due to the different mechanisms [26–28].

*wzhangl@ruc.edu.cn
†daihan@ustc.edu.cn

In this paper, we present a detailed experimental procedure and theoretical analysis of the realization and characterization of the FBL-AL transition in a one-dimensional momentum lattice. The FBL is prepared in a Tasaki lattice with tailored hopping parameters. We demonstrate the localization effect via particle diffusion from a given initial state. Compared to previous works [17], we discuss in detail the procedure and effect of experimental parameter calibration and initial state preparation. We also present a theoretical analysis of the FBL-AL transition, and investigate its detectable signatures in experimentally realistic systems. The results are in good agreement with experimental observations given in Ref. [18].

The remainder of the paper is organized as follows. In Sec. II, we give a detailed introduction to the experimental setup. Starting from the full time-dependent Hamiltonian with two-photon and four-photon Bragg transitions, we derive an effective Hamiltonian in the form of a Tasaki lattice. The experimental parameters are calibrated by the time evolution of particles. The transport property is investigated by the diffusion of particles from a designated initial state. The initialization of such a state is explained in Sec. III. Before the conclusion, we present in Sec. IV the theoretical analysis of the FBL-AL transition and its detectable features with experimental parameters.

II. EXPERIMENTAL SETUP AND TIME-DEPENDENT HAMILTONIAN

In our experiment, we realize the Hamiltonian of a one-dimensional Tasaki lattice,

$$H_{\text{Tasaki}} = \sum_i (u\, \hat{c}_{i,A}^\dagger c_{i,B} + u\, \hat{c}_{i,A}^\dagger \hat{c}_{i+1,B} + \text{H.c.})$$
$$+ \sum_i (v\, \hat{c}_{i,B}^\dagger \hat{c}_{i+1,B} + \text{H.c.}) + \sum_{i,s} W_{i,s} \hat{c}_{i,s}^\dagger \hat{c}_{i,s}, \quad (1)$$

in a momentum-space lattice, where atoms with different linear momenta are considered as designated lattice sites. Here, $\hat{c}_{i,s}^\dagger$ and $\hat{c}_{i,s}$ are the creation and annihilation operators for particles on the $s = A, B$ site of the ith unit cell, $W_{i,s}$ is the on-site energy offset describing a disorder potential, and H.c. stands for the Hermitian conjugate. In the absence of disorder $W_{i,s} = 0$, the single-particle dispersion presents two bands,

$$E_\pm = |v|\cos k \pm \sqrt{|v|^2\cos^2 k + 2|u|^2(1 + \cos k)}. \quad (2)$$

To this aim, we use an optically trapped Bose-Einstein condensate (BEC) of $\sim 6 \times 10^4$ ^{87}Rb atoms with global trapping frequencies $(\omega_x, \omega_y, \omega_y) = 2\pi \times (40, 100, 100)$ Hz. The BEC is driven by a pair of counterpropagating lasers with wavelength $\lambda = 1064$ nm. One of the two lasers has a single frequency component, and the other beam is engineered to contain multiple discrete frequency components, which are chosen to match different two-photon and four-photon Bragg resonance conditions. The laser with a constant wavelength works with each single frequency component of the other beam to resonantly couple a set of momentum states and drive coherent transfer, thus forming a one-dimensional synthetic lattice [9,10] with discrete values of momentum $p_n = 2n\hbar k$, where $k = 2\pi/\lambda$ is the wave vector of the laser and n is the site index. In such a momentum-space lattice, the site-dependent

tunneling strength, tunneling phase, and on-site energy can be independently controlled by modulating the parameters of lasers via a pair of acousto-optic modulators, and various one-dimensional lattice models can be simulated successfully.

Under the rotating wave approximation, the experimental system can be effectively described by the following time-dependent Hamiltonian:

$$H(t) = \sum_n [K(t)\hat{c}_{n+1}^\dagger \hat{c}_n + K^*(t)\hat{c}_n^\dagger \hat{c}_{n+1} + E_n \hat{c}_n^\dagger \hat{c}_n], \quad (3)$$

where $\hat{c}_n$ and $\hat{c}_n^\dagger$ are the annihilation and creation operators of particles on the nth site, respectively, and $E_n = 4n^2 E_r$ is the energy of the nth momentum state according to the free particle energy-momentum dispersion. The hopping coefficient can be written as

$$K(t) = \hbar \sum_j \left(\Omega_{ju} e^{-i\omega_{ju}t} + \Omega_{jv_1} e^{-i\omega_{jv_1}t} + \Omega_{jv_2} e^{-i\omega_{jv_2}t} \right), \quad (4)$$

where the summation over j includes all nearest-neighbor terms (with subscript u) and next-nearest-neighbor terms (v_1 and v_2). The frequency $\omega_{ju} = E_{j+1} - E_j$ denotes the frequency difference between the two laser beams driving the two-photon Bragg transition between nearest-neighboring momentum states. The frequencies ω_{jv_1} and ω_{jv_2} represent the frequency difference between the two laser beams driving the first and second two-photon Bragg transitions of the four-photon Bragg transition between the next-nearest neighbors, respectively, which satisfy $\omega_{jv_1} = (E_{j+2} - E_j)/2 + \delta_j$ and $\omega_{jv_2} = (E_{j+2} - E_j)/2 - \delta_j$, with δ_j being the next-nearest-neighbor detuning configuration parameter.

We can rewrite this time-dependent Hamiltonian in the interaction picture, leading to

$$H_{\text{int}}(t) = \sum_{n,j} \hbar \big[\Omega_{ju} e^{-i(\omega_{ju} - \omega_{nu})t} + \Omega_{jv_1} e^{-i(\omega_{jv_1} - \omega_{nu})t}$$
$$+ \Omega_{jv_2} e^{-i(\omega_{jv_2} - \omega_{nu})t} \big] \hat{c}_{n+1}^\dagger \hat{c}_n + \text{H.c.}. \quad (5)$$

By neglecting the higher-order off-resonant terms [29] and carefully tuning the configuration of δ_j, we can derive an effective Hamiltonian through the second-order perturbative approximation as follows:

$$\tilde{H}_{\text{eff}} = \sum_n t_n^u \hat{c}_{n+1}^\dagger \hat{c}_n + \sum_{n=\text{odd}} t_n^v \hat{c}_{n+2}^\dagger \hat{c}_n + \text{H.c.}. \quad (6)$$

This Hamiltonian corresponds to a zigzag lattice, which contains both nearest- and next-nearest-neighbor hopping terms, and the additional on-site energy can be corrected in numerical simulations and experimental processes. It can be reduced to a Tasaki lattice by turning off the next-nearest-neighbor hopping between sites with even indices.

By carefully tuning the Bragg lasers to make $u = t_n^u$ and $v = t_n^v$, and denoting the momentum states with even (odd) indices as A-sublattice (B-sublattice) sites, this effective model can be finally written as

$$H_{\text{Tasaki}} = \sum_i (u\, \hat{c}_{i,A}^\dagger c_{i,B} + u\, \hat{c}_{i,A}^\dagger \hat{c}_{i+1,B} + \text{H.c.})$$
$$+ \sum_i (v\, \hat{c}_{i,B}^\dagger \hat{c}_{i+1,B} + \text{H.c.}), \quad (7)$$
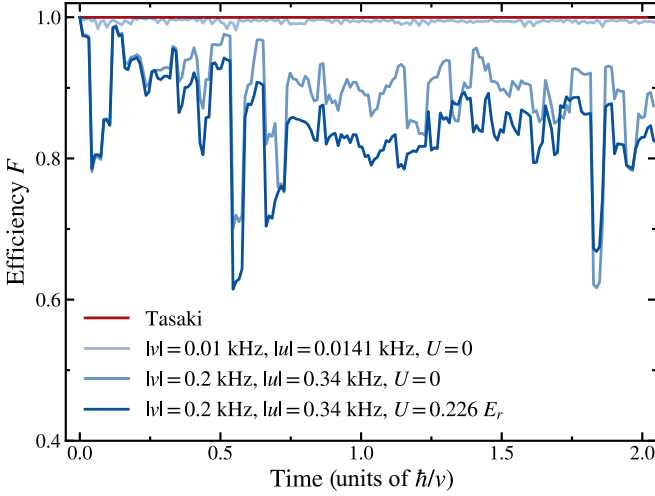
FIG. 1. Simulated time evolution of the efficiency F measuring the distance between the evolved state and a given initial state, under a time-dependent Hamiltonian with different next-nearest tunneling coefficients $|v|$ and interatomic interactions U (blue lines), and an effective Hamiltonian of a Tasaki lattice (red line). The total number of lattice sites is 25, as used in our experiment. The final parameters used in the experiment are $|v| \approx 2\pi\hbar \times 0.2$ kHz, $U = 0.226E_r$, and the optimal u.

which is identical to Eq. (1) with zero disorder strength $W_{i,s} = 0$. A finite disorder potential can be realized by tuning the frequency difference between individual sites.

Since the derivation outlined above is based on a perturbation treatment of intersite tunneling, the resulting effective Hamiltonian should be valid when the tunneling integral is small. However, a small tunneling coefficient also leads to a long characteristic time, which may surpass the coherence time of the system. Thus, one needs to find a suitable parameter range that can validate the effective model and simultaneously allow a short enough time for the system to present characteristic dynamics before losing coherence.

For this purpose, we analyze the dynamical evolution of the system from an initial state, and compare the numerical results of the original time-dependent Hamiltonian Eq. (3) and the effective Tasaki Hamiltonian Eq. (7). When evolving the time-dependent Hamiltonian, we also take into account the interatomic interaction, which is not explicitly included in Eq. (3). We consider an initial state $|\phi_0\rangle = (-\frac{1}{2}|-1\rangle + \frac{\sqrt{2}}{2}|0\rangle - \frac{1}{2}|+1\rangle)$, which is an eigenstate of the flat band of the Tasaki lattice, and calculate the "efficiency" F defined based on the normalized number of atoms $P_n(t)$ detected at each lattice site n and evolving time t [30],

$$F = \left(\sum_n \sqrt{P_n^0 P_n(t)} \right)^2. \qquad (8)$$

Here, $P_n^0 \equiv P_n(t=0)$ is the particle distribution of the initial state. The efficiency parameter characterizes the distance between the evolved state from its origin, and should remain unity if the effective Tasaki model is achieved perfectly.

In Fig. 1, we demonstrate the results of the numerical evolution of Eq. (3) for different choices of the next-nearest
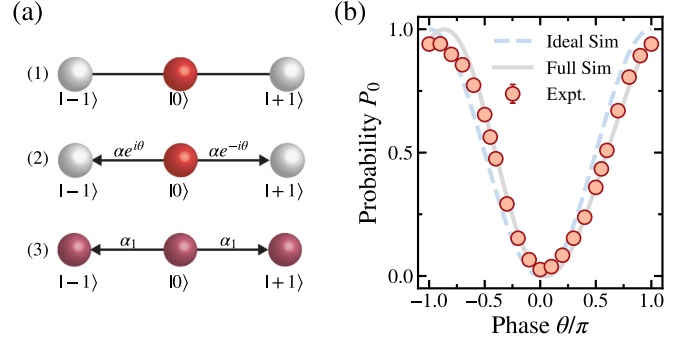
(a)

(b)

FIG. 2. (a) The initial state preparation process. The BEC is first prepared in the zero momentum state (top), and partially transferred to the $|\pm 1\rangle$ states with a proper phase via Bragg processes (middle). The resulting state is then verified by the evolution of particle occupation (bottom). (b) The population of the zero momentum state as a function of phase θ. The best choice of θ can be optimized by this process.

tunneling coefficient $|v|$ and interatomic interaction U (blue lines), in comparison to the case of a perfect Tasaki lattice (red line). The interaction is caused by atomic collisions in synthetic lattices of atomic momentum states [31], and takes the form $U = g\rho = (4\pi\hbar^2 a/M)\rho$ with a as the s-wave scattering length ($\sim 100a_0$ for ^{87}Rb) and ρ as the real-space atomic density. Based on these results, we determine the parameters used in the experiment as $|v| \approx 2\pi\hbar \times 0.2$ kHz and $U \approx 0.226 E_r$, which lead to fast enough dynamics within the system coherence time and tolerable deviation from the perfect scenario.

III. INITIAL STATE PREPARATION

To demonstrate the localization effect, we need to initialize the system at an eigenstate of the flat band of the Tasaki lattice and monitor the time evolution. For a one-dimensional (1D) Tasaki lattice with $r = |u|/|v| = \sqrt{2}$, the eigenstate localized at the ith unit cell reads

$$|\phi_i\rangle = \left(-\frac{1}{2}\hat{c}_{i-1,A}^\dagger + \frac{\sqrt{2}}{2}\hat{c}_{i,B}^\dagger - \frac{1}{2}\hat{c}_{i,A}^\dagger \right)|vac\rangle, \qquad (9)$$

where $|vac\rangle$ is the vacuum state. This state spreads over one B site and two adjacent A sites with equal populations, and can be realized by controlling the strength and phase of nearest-neighbor tunneling in our system [32]. We start from a BEC in the zero momentum state $|0\rangle$, as shown in step (1) of Fig. 2(a). In step (2), a pair of Bragg lasers are applied to drive tunneling between states $|0\rangle$ and $|\pm 1\rangle$, such that particles can be populated to the $|\pm 1\rangle$ states upon evolving. The final state is determined by the strength α, the phase θ, and the duration time t of the Bragg process. In our experiment, we choose $\alpha \approx 2\pi\hbar \times 0.5$ kHz and $t \approx \sqrt{2}/8$ ms for the initial state preparation. It can be easily checked both numerically and experimentally that such choices of α and t can lead to a state with the desired particle population of 1:2:1.

For the tunneling phase θ, a theoretical calculation considering only nearest-neighbor hopping predicts θ should be set at $\pm 0.5\pi$. However, this theoretical suggestion cannot be verified by simply measuring the state population. In fact, the
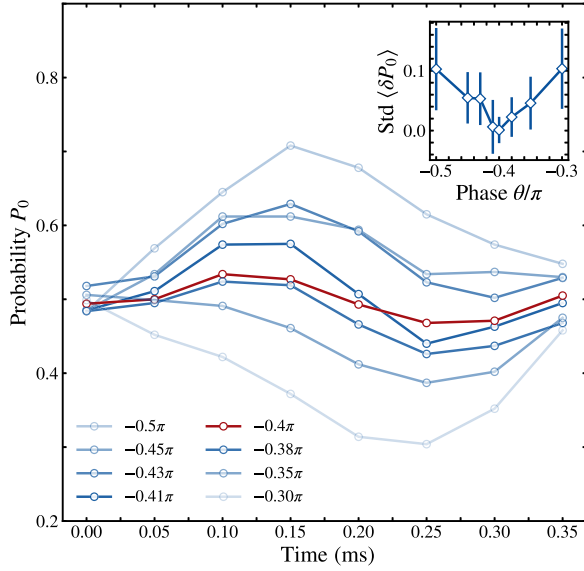
FIG. 3. The population of zero momentum sites as a function of evolution time t_1 under zero-phase Bragg beams. By comparing different values of θ, we notice that the results of $\theta = -0.4\pi$ remain closest to 0.5 for all times, with the smallest variance, as shown in the inset.

FIG. 4. (a) The particle populations (false color) of different sites upon time evolution are measured for cases of $\theta = 0.6\pi$ and -0.4π. (b) The same results obtained from numerical simulation of the time-dependent Hamiltonian Eq. (3). Both panels are taken with $|v| \approx 2\pi\hbar \times 0.2$ kHz and $|u| \approx 2\pi\hbar \times 0.34$ kHz in a Tasaki lattice of 25 sites. (c) The time-averaged efficiency $\langle F \rangle_T$ as a function of the tunneling phase θ. Experimental data (red solid dots with error bars smaller than the size of dots) are averaged over time from $0.75\ \hbar/v$ to $1.5\ \hbar/v$ in steps of $0.0625\ \hbar/v$. The solid gray curve represents a numerical simulation of the time-dependent Hamiltonian with realistic experimental parameters. The maxima of both the experimental and simulation results are approximately $\theta \approx -0.4\pi$.

particle fractions will be the same for all different choices of θ. To determine the correct tunneling phase, we first prepare a state with some specific value of θ, then drive another Bragg process with $\alpha_1 \approx 2\pi\hbar \times 0.5$ kHz and $\theta = 0$ on the prepared state and measure the particle occupation on different sites after an evolving time t_1. This process is shown as step (3) in Fig. 2(a). If the state is prepared perfectly as $|\phi_0\rangle$, one can easily show that the particle fractions on $|-1\rangle$, $|0\rangle$, and $|+1\rangle$ should be fixed at 1:2:1 during the whole evolution process. Specifically, the atomic probability of the $|0\rangle$ momentum state should be a constant of $P_0 = 0.5$ owing to the completely destructive interference of hopping to the two neighboring sites. However, if the state is prepared with some error, P_0 will deviate from 0.5 and vary over time.

In Fig. 2(b), we present the results of $P_0(t_1)$ after an evolution of $t_1 \approx \sqrt{2}/8$ ms after the zero-phase Bragg process for several choices of θ. The experimental data (red solid dots) agree well with the numerical simulation (gray solid lines), showing that $P_0 \approx 0.5$ when $\theta \approx -0.4\pi$ and 0.6π. This observation is slightly different from the theoretical prediction $\pm 0.5\pi$. The deviation can be attributed to the presence of interatomic interactions as well as nonidealities. We then fine-tune θ around -0.4π and measure $P_0(t_1)$ for $t_1 \lesssim \sqrt{2}/4$ ms $\approx$ 0.35 ms. As shown in Fig. 3, the results for $\theta \approx -0.4\pi$ are always close to the expected value of $P_0 \approx 0.5$, with the smallest variance as depicted in the inset.

We further observe the whole evolution process for states prepared with different θ in the Tasaki flat-band system. In Figs. 4(a) and 4(b), we present the experimental data and numerical simulations of $\theta = -0.4\pi$ and 0.6π. The results show an obvious localization effect for $\theta = -0.4\pi$, where the major population is kept within the center three-momentum states during the evolution. We calculate the time-averaged
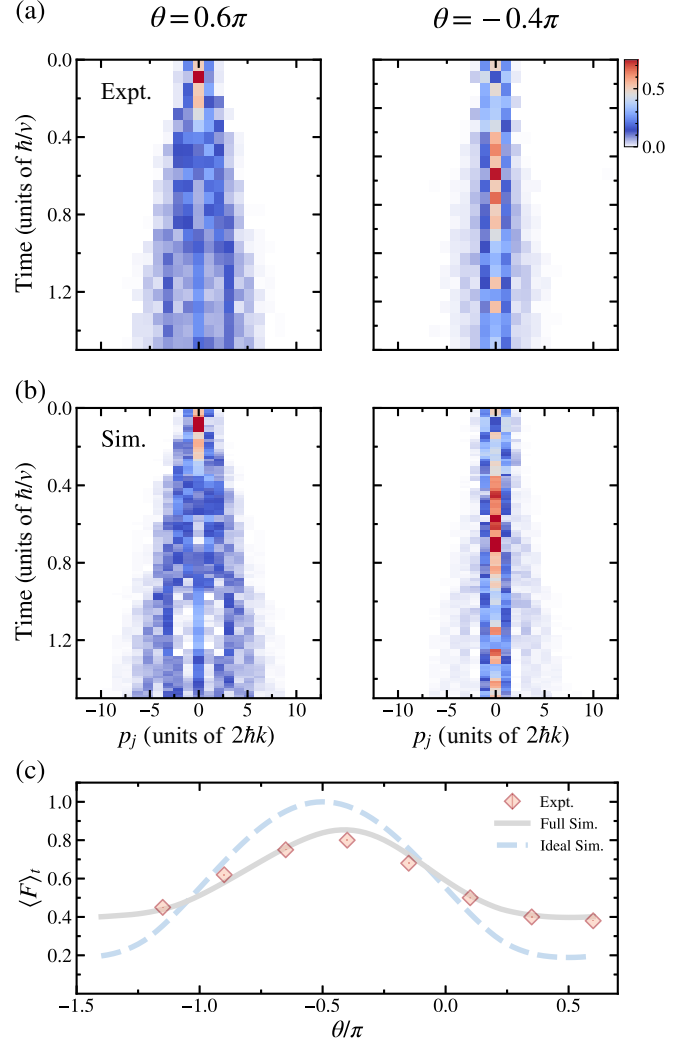
efficiency $\langle F \rangle_T$ based on the definition below [30]:

$$F_m = \left(\sum_n \sqrt{P_n^{m,\text{Tasaki}} P_n^{m,\text{expt}}} \right)^2, \qquad (10)$$

where the results for a Tasaki lattice $P_n^{m,\text{Tasaki}}$ and for the experimental system $P_n^{m,\text{expt}}$ are both used. As shown in Fig. 4(c), the experimental data for $\theta \approx -0.4\pi$ are mostly localized and in good agreement with the numerical simulation of the time-dependent Hamiltonian. With all these results, we set $\theta \approx -0.4\pi$ to prepare the initial state $|\phi_0\rangle$.

IV. LEVEL SPACING ANALYSIS AND EXPERIMENTAL SIGNATURES

A system containing nondispersive bands features localized eigenstates referred to as compact localized states. If the flat band is separated from other dispersive bands by a gap, the localized states are robust against weak disorder, and lead to a nonconductive phase usually referred to as flat-band localization (FBL). When disorder is sufficiently strong, it can suppress the propagation of waves and induce Anderson localization (AL). Thus, for a flat-band system, such as the Tasaki lattice, a transition from FBL to AL is expected with increasing disorder. In this section, we analyze the properties of eigenvalues and single-particle wave functions to study the competition between two kinds of localizations. In the calculation below, we use W to represent the dimensionless disorder strength in units of $|v|$ with $W_{i,s} = m_{i,s}W|v|$, where $m_{i,s}$ is a random number uniformly distributed within $[-1, 1]$.

The level-spacing ratio and level-spacing distribution can be obtained from the single-particle energy spectrum of the disordered Hamiltonian. The level-spacing ratio r is defined as [24,27]

$$r = \frac{1}{N-1} \sum_{j=1}^{N-1} \frac{\min[s_j, s_{j+1}]}{\max[s_j, s_{j+1}]}, \tag{11}$$

where the energy level spacing $s_j = E_{j+1} - E_j$, and E_j is the single-particle energy of the jth eigenstate in ascending order. We consider only the lower half of the eigenenergies to calculate the level-spacing ratio, which is kept close to 0.386 as shown in Fig. 5(a). Figure 5(b) depicts the level-spacing distribution for an intermediate disorder strength $W = 2$, which has a Poisson form with $P(s) = e^{-s}$. In fact, the level-spacing distribution takes a Poisson structure across the entire range of disorder strength. The results of the level-spacing ratio and distribution both indicate that the system stays in a localized phase for the entire disorder strength range.

For the eigenstate properties, we consider the inverse participation ratio (IPR) of the jth normalized single-particle eigenstate $|\psi_j\rangle$ defined as [24,27]

$$\mathcal{I}_j = \sum_{i=1}^{N} |\psi_j(i)|^4, \tag{12}$$

where $\psi_j(i)$ is the wave function at site i. Apparently, $\mathcal{I}_j$ is unity for a single-site localized state, while for a perfectly delocalized state it scales as $1/N$. In the presence of disorder, we can further define an average IPR $\tilde{\mathcal{I}}$ over all eigenstates of the system, and show the result with varying disorder W. As depicted in Fig. 5(c), the average IPR shows distinct behaviors in the FBL phase with weak disorder and the AL phase with strong disorder. The transition takes place around $W \approx 2$, which corresponds to the energy gap between the flat and neighboring dispersive bands of the Tasaki lattice.

The von Neumann entropy can provide further evidence for the FBL-AL transition. The definition of von Neumann entropy of site i in the jth eigenstate reads [24]

$$\mathcal{S}_j^i = -|\psi_j(i)|^2 \log_2(|\psi_j(i)|^2) \\ - (1 - |\psi_j(i)|^2) \log_2(1 - |\psi_j(i)|^2). \tag{13}$$
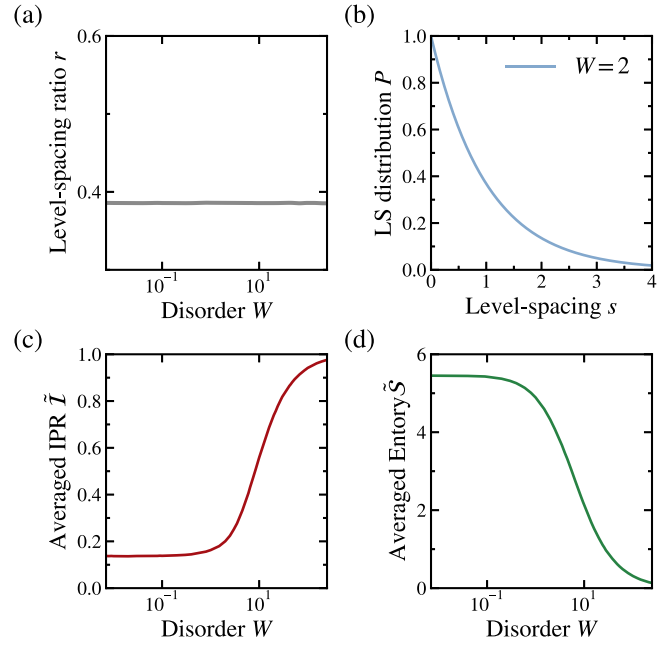

FIG. 5. (a) The level-spacing ratio of the lower half of single-particle eigenenergies versus disorder. (b) The lower half level-spacing (LS) distribution with disorder strength $W = 2$. (c) The average IPR of all single-particle eigenstates. (d) The von Neumann entropy averaged over all eigenstates. The results are obtained for a system of size $N = 1001$ and averaged over 100 configurations of disorder.

It is very clear that for a single-site localized state, $\mathcal{S}_j^i = 0$, while in a delocalized state with $|\psi_j(i)|^2 = 1/N$, $\mathcal{S}_j^i \approx (1/N)\log_2 N + 1/N$. By averaging over all eigenstates and all sites of the system, the average von Neumann entropy

$$\tilde{\mathcal{S}} = \frac{\sum_{j=1}^{N} \left(\sum_i \mathcal{S}_j^i\right)}{N} \tag{14}$$

remains zero if all eigenstates are localized within a single site, and approaches $\tilde{\mathcal{S}} \approx (\log_2 N + 1)$ if all eigenstates are delocalized. In Fig. 5(d), we show the numerical result of $\tilde{\mathcal{S}}$ for a system with size $N = 1001$. Notice that the average von Neumann entropy is always less than the delocalized limit for all disorder strengths, and shows distinct behaviors in FBL and AL phases.

We further investigate the localization length ξ, which is defined from the asymptotic exponential decay of a localized state wave function [20–23],

$$\psi_j^{n,\alpha} \propto \exp(-n/\xi), \tag{15}$$

which correlates to the subsite $\alpha = A, B$ in the nth unit cell. To calculate the localization length, we start from the Schrödinger equation of the Tasaki lattice,

$$i\dot{b}_n + W_{n,b}b_n = -|v|(b_{n-1} + b_{n+1}) - |u|(a_n + a_{n-1}),$$
$$i\dot{a}_n + W_{n,a}a_n = -|u|(b_n + b_{n+1}), \tag{16}$$

where a_n and b_n denote coefficients of the wave function at the A and B sites within the nth cell, respectively. Assuming $\{a_n(t), b_n(t)\} = \{a_n, b_n\}e^{iEt}$ with E the eigenenergy, the solution of the Schrödinger equation can be formally
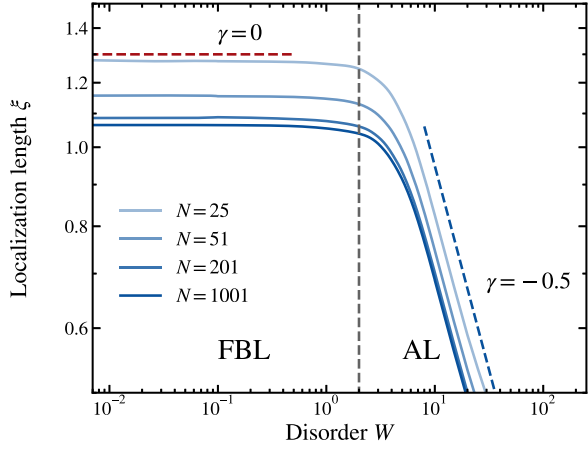
FIG. 6. Localization length for the eigenstate of $E = -2|v|$ in a system of size $N = 25, 51, 201, 1001$ (from top to bottom). The average time of disorder configurations $|W_{i,s}| < W$ is at least 100, where we apply more disorder configurations for smaller sizes. The power-law exponent γ changes from 0 in the FBL limit to -0.5 in the AL limit for all system sizes.

written as

$$a_n = \frac{|u|(b_n + b_{n+1})}{E - W_{n,a}},$$

$$\epsilon_n b_n = C_n b_{n+1} + C_{n-1} b_{n-1}, \qquad (17)$$

with parameters

$$\epsilon_n = E - W_{n,b} - |u|^2 \left(\frac{1}{E - W_{n,a}} + \frac{1}{E - W_{n-1,a}} \right),$$

$$C_n = |v| + |u|^2 \frac{1}{E - W_{n,a}}. \qquad (18)$$

By solving the equations above numerically, we can extract the localization length via

$$\xi^{-1}(E) = \lim_{N \to \infty} \frac{1}{(N-1)/2} \left\langle \sum_{n=1}^{(N-1)/2} \ln \left| \frac{b_{n+1}}{b_n} \right| \right\rangle, \qquad (19)$$

where $(N-1)/2$ is the number of unit cells. The result of the localization length shown in Fig. 6 also suggests that there is a transition between FBL and AL. The transition point is almost the same for different system sizes ranging from $N = 25$ to 1001. Specifically, two different power-law behaviors $\xi(W) \sim W^\gamma$ can be observed in the weak and strong disorder regions. In the weak disorder limit, ξ is nearly a constant with $\gamma = 0$. In the strongly disordered region, the exponent $\gamma \approx -0.5$. Based on these results, we find that the FBL-AL transition occurs when the disorder strength approaches the band gap $W \approx 2$ [23].

We display in Fig. 7(a) a false-colored plot of $\langle F \rangle$ obtained by simulation with varying r and W, where the FBL phase (i) is separated from the AL phase (iii) by a transition region (ii). The result also shows that the best u/v is $\sqrt{2}$ for the Tasaki flat-band lattice. In Figs. 7(b)–7(d), we present the disorder-averaged efficiency F, IPR, and von Neumann entropy for a single state after time evolution simulated with the effective Hamiltonian Eq. (1), where we can observe
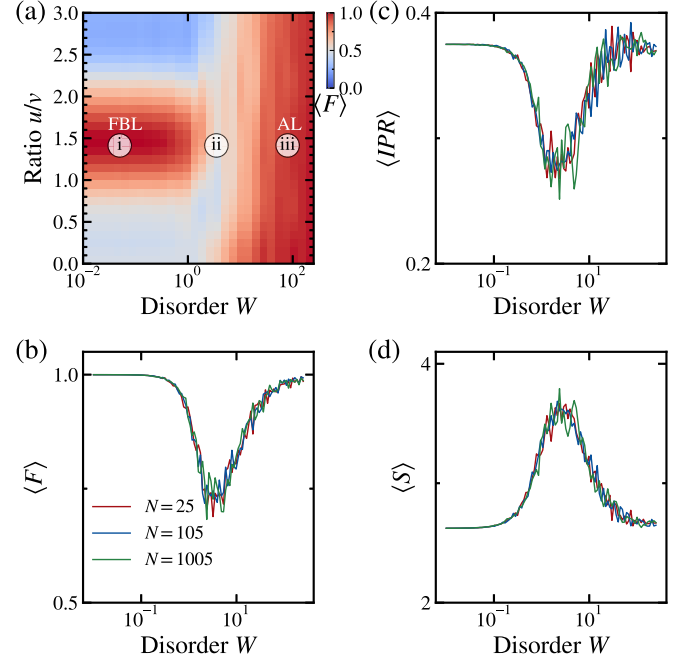

FIG. 7. (a) False-colored plot of the disorder averaged efficiency $\langle F \rangle$ obtained from numerical simulation of Eq. (1) for $t = 2.125\hbar/|v|$. By varying the disorder strength W and the hopping ratio r, two localized regions (red) labeled by (i) and (iii) can be identified and are separated by a crossover region labeled by (ii). (Color online) Simulation of the efficiency (b), IPR (c), and von Neumann entropy (d) of a single state after evolving upon the effective Tasaki lattice model. Different lines denote results for different sizes $N = 25$ (red), 105 (blue), and 1005 (green). The initial state is chosen as an eigenstate of the flat band in the Tasaki lattice. All simulations are taken with $|v| = 2\pi\hbar \times 0.2$ kHz and $|u| = 2\pi\hbar \times 0.282$ kHz.

clear signatures (dip or peak) across the FBL-AL transition. Since the initial state is an eigenstate of the flat-band model, the final state is still close to the initial state owing to the destructive interference of flat-band hopping when disorder is small, and the physical observables almost remain at their FBL limits. As disorder approaches the band gap, i.e., $W \approx 2$, the destructive interference is strongly destroyed, such that the final state is significantly changed to leave some signatures in observables. As disorder is further enhanced, intersite hopping is almost forbidden and the system is again kept at its initial state. We assume that the signatures found around $W \approx 2$ denote a switch of localization mechanism, i.e., an FBL-AL transition, whose position is determined by the size of the energy gap and independent of the system size.

V. CONCLUSION

In this work, we present a comprehensive experimental realization of a Tasaki lattice in a momentum lattice platform. The momentum lattice is constructed by an optically trapped BEC comprising approximately 6×10^4 ^{87}Rb atoms, subjected to the influence of a pair of counterpropagating lasers. Through precise adjustments to the frequency and phase of the lasers, ensuring resonance conditions for two-photon and four-photon Bragg processes, we achieve coherent transfer

between the nearest- and next-nearest-neighbor momentum states. We also show the method for preparing the flat-band eigenstate of the Tasaki lattice. Ultimately, we offer a theoretical analysis of this system. The behavior of the IPR and von Neumann entropy, averaged over all eigenstates, manifests distinct patterns in weak and strong disorder limits, indicating the presence of two different localization mechanisms. Notably, the transition from FBL to AL states is clearly discernible through the scaling behavior of the localization length. Additionally, theoretical simulations of single state properties reveal that the FBL-AL transition remains independent of the system size. One of the most powerful advantages of the momentum lattice platform lies in its capability for precise control of tunneling between different sites as well as the on-site energy of individual sites. In the future, we firmly believe that our method holds significant promise for successfully observing exotic topological [33,34] and transport properties [17,35] in diverse lattice structures. This opens the door to a broader range of study options, broadening our understanding of quantum systems and paving the way for innovative investigations in related fields.

[1] K. Bian, C. Gerber, A. J. Heinrich, D. J. Müller, S. Scheuring, and Y. Jiang, Nat. Rev. Methods Primers **1**, 36 (2021).

[2] S. de Léséleuc, V. Lienhard, P. Scholl, D. Barredo, S. Weber, N. Lang, H. P. Büchler, T. Lahayeo, and A. Browaeys, Science **365**, 775 (2019).

[3] B. M. Spar, E. Guardado-Sanchez, S. Chi, Z. Z. Yan, and W. S. Bakr, Phys. Rev. Lett. **128**, 223202 (2022).

[4] A. M. Kaufman and K.-K. Ni, Nat. Phys. **17**, 1324 (2021).

[5] D. Wei, D. Adler, K. Srakaew, S. Agrawal, P. Weckesser, I. Bloch, and J. Zeiher, Phys. Rev. X **13**, 021042 (2023).

[6] H.-Y. Wang, W.-Y. Zhang, Z. Yao, Y. Liu, Z.-H. Zhu, Y.-G. Zheng, X.-K. Wang, H. Zhai, Z.-S. Yuan, and J.-W. Pan, Phys. Rev. Lett. **131**, 050401 (2023).

[7] C. Weitenberg, M. Endres, J. F. Sherson, M. Cheneau, P. Schauß, T. Fukuhara, I. Bloch, and S. Kuhr, Nature (London) **471**, 319 (2011).

[8] W.-Y. Zhang, M.-G. He, H. Sun, Y.-G. Zheng, Y. Liu, A. Luo, H.-Y. Wang, Z.-H. Zhu, P.-Y. Qiu, Y.-C. Shen, X.-K. Wang, W. Lin, S.-T. Yu, B.-C. Li, B. Xiao, M.-D. Li, Y.-M. Yang, X. Jiang, H.-N. Dai, Y. Zhou *et al.*, Phys. Rev. Lett. **131**, 073401 (2023).

[9] B. Gadway, Phys. Rev. A **92**, 043606 (2015).

[10] F. A. An, E. J. Meier, and B. Gadway, Phys. Rev. X **8**, 031045 (2018).

[11] W. Gou, T. Chen, D. Xie, T. Xiao, T.-S. Deng, B. Gadway, W. Yi, and B. Yan, Phys. Rev. Lett. **124**, 070402 (2020).

[12] E. J. Meier, F. A. An, and B. Gadway, Nat. Commun. **7**, 13986 (2016).

[13] E. J. Meier, F. A. An, A. Dauphin, M. Maffei, P. Massignan, T. L. Hughes, and B. Gadway, Science **362**, 929 (2018).

[14] D. Xie, T.-S. Deng, T. Xiao, W. Gou, T. Chen, W. Yi, and B. Yan, Phys. Rev. Lett. **124**, 050502 (2020).

[15] Y. Li, H. Du, Y. Wang, J. Liang, L. Xiao, W. Yi, J. Ma, and S. Jia, Nat. Commun. **14**, 7560 (2023).

[16] Z. Dong, H. Li, T. Wan, Q. Liang, Z. Yang, and B. Yan, Nat. Photon. **18**, 68 (2024).

[17] H. Li, Z. Dong, S. Longhi, Q. Liang, D. Xie, and B. Yan, Phys. Rev. Lett. **129**, 220403 (2022).

[18] C. Zeng, Y.-R. Shi, Y.-Y. Mao, F.-F. Wu, Y.-J. Xie, T. Yuan, W. Zhang, H.-N. Dai, Y.-A. Chen, and J.-W. Pan, companion paper, Phys. Rev. Lett. **132**, 063401 (2024).

[19] P. W. Anderson, Phys. Rev. **109**, 1492 (1958).

[20] B. Kramer and A. MacKinnon, Rep. Prog. Phys. **56**, 1469 (1993).

[21] D. Leykam, S. Flach, O. Bahat-Treidel, and A. S. Desyatnikov, Phys. Rev. B **88**, 224203 (2013).

[22] S. Flach, D. Leykam, J. D. Bodyfelt, P. Matthies, and A. S. Desyatnikov, Europhys. Lett. **105**, 30001 (2014).

[23] D. Leykam, J. D. Bodyfelt, A. S. Desyatnikov, and S. Flach, Eur. Phys. J. B **90**, 1 (2017).

[24] N. Roy, A. Ramachandran, and A. Sharma, Phys. Rev. Res. **2**, 043395 (2020).

[25] T. Orito, Y. Kuno, and I. Ichinose, Phys. Rev. B **104**, 094202 (2021).

[26] C. Monthus and T. Garel, Phys. Rev. B **81**, 134202 (2010).

[27] Y. Kuno, T. Orito, and I. Ichinose, New J. Phys. **22**, 013032 (2020).

[28] Y. Wang, C. Cheng, X.-J. Liu, and D. Yu, Phys. Rev. Lett. **126**, 080602 (2021).

[29] E. Giese, A. Roura, G. Tackmann, E. M. Rasel, and W. P. Schleich, Phys. Rev. A **88**, 053608 (2013).

[30] E. J. Meier, K. Ngan, D. Sels, and B. Gadway, Phys. Rev. Res. **2**, 043201 (2020).

[31] F. A. An, B. Sundar, J. Hou, X.-W. Luo, E. J. Meier, C. Zhang, K. R. A. Hazzard, and B. Gadway, Phys. Rev. Lett. **127**, 130401 (2021).

[32] D. Linnemann, H. Strobel, W. Muessel, J. Schulz, R. J. Lewis-Swan, K. V. Kheruntsyan, and M. K. Oberthaler, Phys. Rev. Lett. **117**, 013001 (2016).

[33] M. Kremer, I. Petrides, E. Meyer, M. Heinrich, O. Zilberberg, and A. Szameit, Nat. Commun. **11**, 907 (2020).

[34] Z.-Q. Jiao, S. Longhi, X.-W. Wang, J. Gao, W.-H. Zhou, Y. Wang, Y.-X. Fu, L. Wang, R.-J. Ren, L.-F. Qiao, and X.-M. Jin, Phys. Rev. Lett. **127**, 147401 (2021).

[35] G. Cáceres-Aravena, D. Guzmán-Silva, I. Salinas, and R. A. Vicencio, Phys. Rev. Lett. **128**, 256602 (2022).